



LAWRENCE
LIVERMORE
NATIONAL
LABORATORY

A buoyancy-shear-drag-based turbulence model for Rayleigh-Taylor, reshocked Richtmyer-Meshkov, and Kelvin-Helmholtz mixing

O. Schilling

July 13, 2019

Physica D

Disclaimer

This document was prepared as an account of work sponsored by an agency of the United States government. Neither the United States government nor Lawrence Livermore National Security, LLC, nor any of their employees makes any warranty, expressed or implied, or assumes any legal liability or responsibility for the accuracy, completeness, or usefulness of any information, apparatus, product, or process disclosed, or represents that its use would not infringe privately owned rights. Reference herein to any specific commercial product, process, or service by trade name, trademark, manufacturer, or otherwise does not necessarily constitute or imply its endorsement, recommendation, or favoring by the United States government or Lawrence Livermore National Security, LLC. The views and opinions of authors expressed herein do not necessarily state or reflect those of the United States government or Lawrence Livermore National Security, LLC, and shall not be used for advertising or product endorsement purposes.

A buoyancy–shear–drag-based turbulence model for Rayleigh–Taylor, reshocked Richtmyer–Meshkov, and Kelvin–Helmholtz mixing

Oleg Schilling

Lawrence Livermore National Laboratory, P.O. Box 808, Livermore, CA 94550, USA

Abstract

A phenomenological turbulence model for Rayleigh–Taylor, reshocked Richtmyer–Meshkov, and Kelvin–Helmholtz instability-induced mixing is developed using a general buoyancy–shear–drag model. Analytical solutions to the model equations corresponding to each instability are derived separately, which are then used to calibrate the model coefficients to predict specific values of the mixing growth parameters and exponents. The buoyancy–shear–drag equations for the bubble and spike mixing layer widths are then solved numerically, and a turbulent diffusivity (or viscosity) is constructed dimensionally as the product of the mixing layer width, h , and its time-derivative, dh/dt . Surrogate turbulent fields are then constructed by multiplying a presumed self-similar spatial profile by appropriate functions of h and dh/dt . Using several simplifying approximations, the turbulent diffusion equations satisfied by the mean mass fraction and mean shear velocity are solved analytically in a reference frame moving with the mean advection velocity. The turbulent diffusivity (and corresponding viscosity) are used in the analytical expressions, and it is shown that the mean fields evolve in space and time as expected. *The explicit modeling and solution of turbulent transport equations (e.g., for the turbulent kinetic energy and its dissipation rate or a lengthscale) are not required.* By using separate equations for the bubble and spike evolution, the model naturally captures the asymmetry induced by an increasing density contrast between the heavy and light fluids. The model also includes molecular dissipation and diffusion, and therefore, can describe transition to fully-developed turbulence if the initial turbulent diffusivity/viscosity are much smaller than the molecular diffusivity/viscosity. This model is applied to constant-acceleration Rayleigh–Taylor, impulsively reshocked Richtmyer–Meshkov, and constant density Kelvin–Helmholtz mixing layers to demonstrate its utility. It is shown that the numerical solutions of the model calibrated using specific values of the instability growth parameters and exponents: (1) produces mixing layer widths in agreement with the expected self-similar growth power laws; (2) gives spatiotemporal profiles of turbulent fields that are expected and consistent with previous results; (3) predicts the expected power-law growths and decays of the spatially-integrated turbulent fields, and; (4) gives spatiotemporal profiles of the mean fields that are expected and consistent with previous results. This relatively simple model can be implemented numerically, and is expected to be useful for fundamental as well as astrophysical and inertial confinement fusion applications.

Keywords: Turbulent mixing, buoyancy–drag, Rayleigh–Taylor, Richtmyer–Meshkov, Kelvin–Helmholtz, reshock

1. Introduction

Turbulence and turbulent mixing exist in a multitude of flows in nature and applied science. Although considerable progress has been made in better understanding turbulent mixing using numerical simulations and experiments, the modeling of the impact of turbulent mixing on the hydrodynamic evolution of many flows of interest remains challenging. This is particularly true for complex flows in which the hydrodynamics is coupled to other physics such as radiation and particle transport. Many of these flows are density-stratified or consist of multiple materials (or fluids), and are subject to unstable growth at perturbed interfaces (such as in layers in a star or in an inertial confinement fusion target) induced by accelerations, shocks, and shear—Rayleigh–Taylor, Richtmyer–Meshkov, and Kelvin–Helmholtz instabilities, respectively (see

[1] for a recent review). Such flows can also be subject to stable conditions, which reduce turbulence (often referred to as ‘demixing’) and should be accounted for in any credible turbulence model.

Considerable effort has been employed to develop increasingly more complete and necessarily more complex turbulent transport (i.e., Reynolds-averaged) models to describe the effects of turbulence and mixing on mean hydrodynamic flow fields. In addition to developing more physically complete and correct closures for the terms in the equations that produce turbulence, much effort has been made to calibrate these models using key quantities measured (or inferred) from experiments and numerical simulations (e.g., direct numerical, large-eddy, and implicit large-eddy simulations). In many applications in which turbulence is one of many competing, nonlinear physical effects to be modeled, there remains a need to incorporate turbulent mixing in a computationally economical manner and using models that are relatively easily implemented in highly com-

Email address: schilling1@llnl.gov (Oleg Schilling)

plex multiphysics codes such as supernova explosion codes [2] and inertial confinement fusion codes [3]—despite considerable progress, the role of mixing in these representative applications remains relatively poorly understood.

A considerably simpler method to estimate the spatial extent of mixing is based on buoyancy–drag modeling [4–8], in which ordinary differential equations are solved for the heavy (i.e., “spike”) and light (i.e., “bubble”) mixing fronts based on the assumption of binary mixing across an interface. Reynolds-averaged models are more complex, as they evolve partial differential equations for fields in space and time, although these equations can be treated in a much simpler form by spatially integrating them over the mixing layer to obtain ordinary differential equation models [9]. Buoyancy–drag models also offer a relatively simple methodology to understand the basic growth characteristics of mixing layers, and have been utilized for modeling the growth of fundamental single- and multimode Rayleigh–Taylor and Richtmyer–Meshkov instabilities [10–32], modeling instability growth in high-energy-density experiments [33–41], modeling blast-wave-driven instability growth relevant to supernovae [42–45], and modeling multiphase Rayleigh–Taylor and Richtmyer–Meshkov instabilities in dusty gases [46–48] (see Refs. [49, 50] for a review). A two-scale K – ϵ turbulence model coupled to a buoyancy–drag model was developed for mixing induced by Rayleigh–Taylor and Richtmyer–Meshkov instabilities [51]. Source and sink terms based on the buoyancy–drag equations were developed to describe the self-similar growth of Rayleigh–Taylor and Richtmyer–Meshkov mixing using a K – L turbulence model [52].

Motivated by the considerations outlined above, the objective of the present work is to suitably generalize buoyancy–drag and shear–drag models to turbulence models by hybridizing the solutions of these models with presumed self-similar profiles for turbulent fields. This methodology utilizes the fact that the mean flow equations (typically, the mean mass fraction and mean shear velocity equations) transformed into a reference frame moving with the mean velocity, become turbulent diffusion equations that can be solved analytically using suitable approximations or numerically more generally. The turbulent diffusion terms are closed using the standard gradient-diffusion approximation, requiring a turbulent viscosity or diffusivity.

In a traditional turbulent transport modeling paradigm, a turbulent kinetic energy and at least one additional mechanical turbulence equation are solved to obtain the turbulent viscosity, which in turn is used to model the effects of turbulence as a diffusive process. In the model developed here, the turbulent viscosity is constructed as a spatial profile by:

1. solving the buoyancy–shear–drag equations for the bubble and spike mixing layer widths h_b and h_s ,
2. using the total mixing width $h = h_b + h_s$ and its rate of change dh/dt to obtain a time-dependent turbulent diffusivity and viscosity $D_i, \nu_i \propto h dh/dt$, and;
3. constructing a space–time turbulent diffusivity or viscosity by multiplying the time-dependent value by a self-similar profile of the form $f(\eta)$, where $\eta \propto z/h(t)$ is the similarity

variable (z is the coordinate along the direction of acceleration or shock).

The resulting turbulent diffusivity or viscosity is used for gradient-diffusion closures of the mean flow equations or is substituted directly into approximate analytic expressions for the mean fields, which can then be evolved in space and time. Thus, the model does not require the solution of auxiliary turbulent transport equations, which require closure modeling of many terms and a robust numerical implementation. The present model only requires the integration of ordinary differential equations with, for example, analytically specified or numerical value of the acceleration (as obtained self-consistently from a simulation).

This paper is organized as follows. In Sec. 2 the buoyancy–shear–drag equations are formulated in a unified manner to include all three instabilities. The equations are then solved separately for each instability (for constant and impulsive accelerations) analytically, and the model coefficients are calibrated using specific values of the instability growth parameters and exponents. The model equations are then solved numerically for representative Rayleigh–Taylor, reshocked Richtmyer–Meshkov, and Kelvin–Helmholtz mixing layer cases in Sec. 3, 4, and 5, respectively. The broader application of the model is briefly discussed in Sec. 6. Finally, a summary of the modeling methodology, principal results, and conclusions are given in Sec. 7.

2. The generalized buoyancy–shear–drag turbulence model

The generalized buoyancy–shear–drag model equations for the ‘bubble’ and ‘spike’ mixing layer fronts are formulated and discussed here, together with the phenomenological construction of the turbulent diffusivity/viscosity required later to close the mean flow equations. The model equations combine elements from previously developed buoyancy–drag models.

2.1. Formulation of the buoyancy–shear–drag equations

Consider a two- or three-dimensional, two-fluid flow consisting of bubbles and spikes in an effective gravitational field $g_{\text{eff}}(t)$ and including velocity shear Δv . The densities are $\rho_s = \rho_1$ and $\rho_b = \rho_2 < \rho_1$. Thus, with bubbles and spikes corresponding to $i = 1$ and $i = 2$, respectively, the Newton second law equations of motion for the bubble and spike are

$$\rho_{3-i} \frac{dv_{3-i}}{dt} = F_b^{3-i} + F_s^{3-i} + F_{vm}^{3-i} + F_d^{3-i} + F_{abl}^{3-i} \quad (1)$$

with the buoyancy force, shear force, virtual mass (plus pressure) force, drag force, and ablative-stabilization force

$$F_b^{3-i}(t) = C_b [1 - E(t)] (\rho_1 - \rho_2) g_{\text{eff}}(t), \quad (2)$$

$$F_s^{3-i}(t) = C_s \frac{\rho_i^2 \rho_{3-i}}{(\rho_i + \rho_{3-i})^2} \frac{(\Delta v)^2}{\ell_{3-i}(t) \delta_{i2} + \ell_i(t) \delta_{i1}}, \quad (3)$$

$$F_{vm}^{3-i}(t) = -\{C_{vm} E(t) \rho_{3-i} + [C_{vm}^* + E(t)] \rho_i\} \frac{dv_{3-i}}{dt}, \quad (4)$$

$$F_d^{3-i}(t) = -\frac{C_d}{b} \frac{\rho_i |v_{3-i}(t)|}{\ell_{3-i}(t)} \quad (5)$$

$$\times \sqrt{\left\{ \left[R_i^n \delta_{i1} + R_i \left(\frac{h_{3-i}}{h_i} \right)^\beta \delta_{i2} \right] v_{3-i}(t) \right\}^2 + (\Delta v)^2},$$

$$F_{abl}^{3-i}(t) = -C_a \frac{\rho_i v_a |v_{3-i}(t)|}{\ell_{3-i}(t)}, \quad (6)$$

respectively. The characteristic bubble and spike lengthscale (i.e., radius) is [53]

$$\ell_{3-i}(t) \equiv \frac{V_{3-i}(t)}{b S_{3-i}(t)} = h_{3-i}(t) \quad (7)$$

for multimode mixing and

$$\ell_{3-i}(t) \equiv \lambda(t) \quad (8)$$

for single-mode evolution with geometrical factor b (e.g., in three dimensions, $V^{3-i} = 4\pi\ell_{3-i}^3/3$ and $S^{3-i} = 2\pi\ell_{3-i}^2$, so that $b = 2/3$; in two dimensions, $V^{3-i} = 2\pi\ell_{3-i}^2$ and $S^{3-i} = 2\pi\ell_{3-i}$, so that $b = 1$). Note that the surface-to-volume ratio is $S_{3-i}(t)/V_{3-i}(t) = 1/(b\ell_{3-i})$. Equation (1) predicts decay rather than growth if $dv_{3-i}/dt < 0$.

This model depends on five dimensionless coefficients C_b , C_s , C_{vm} ($C_{vm}^* = C_{vm} + 1$ accounts for the pressure gradient force), C_d , and C_a , and two parameters n and $\beta > 0$; the factor $R_i = \rho_i/(\rho_i + \rho_{3-i})$ introduces a density dependence in the drag terms, and $[h_s(t)/h_b(t)]^{2\beta}$ increases the drag on the spikes as the spike to bubble amplitude ratio increases [15]. The linear electric motor instability growth experiments with impulsive accelerations are best fit with $n = 0$, and the Vetter–Sturtevant shock tube experiments are best fit with $\beta = 1$ [15]. When $\Delta v = 0$, these equations describe Rayleigh–Taylor and Richtmyer–Meshkov instability-induced mixing. Bubbles and spikes do not generally have well-defined frontal areas and volumes. The dominant bubble and spike can be regarded as coherent, large-scale structures in a mixing-length approximation.

The exponential factor in Eqs. (2) and (4) is [21]

$$E(t) = \exp[-C_e k h_b(t)] \quad (9)$$

with $C_e = 3$ and 2 for two and three dimensions, respectively; at large times, $E(t) \downarrow 0$, and the conventional equations are recovered. For small times, $E(t) \approx 1 - C_e k h_b(t)$. In the single-mode case, $\lambda(t)$ is given by an expression of the form [14]

$$\lambda(t) = \max[\lambda_0, b|h| + (1 - m b)\lambda_0], \quad (10)$$

where m is a parameter, or is determined by solving a differential equation [21]. In the multimode case, k can be interpreted as an rms wavenumber. In the model applications to multimode mixing layer fronts below, $E(t) = 0$.

The bubble and spike velocity in an incompressible flow is

$$v_{3-i}(t) = \frac{dh_{3-i}}{dt}, \quad (11)$$

where the *effective mixing-length* h_{3-i} is the bubble and spike amplitude satisfying the initial condition $h_{3-i}(0) = h_{0,i}$. In a compressible flow v_{3-i} are bubble and spike velocities relative to the fluid, so that Eq. (11) is generalized to [13]

$$v_{3-i}(t) = \frac{dh_{3-i}}{dt} + (-1)^{i+1} [u_{3-i}(t) - u_{int}(t)], \quad (12)$$

where u_1 , u_2 , and u_{int} are the velocities at $z_{int} + h_b$, $z_{int} - h_s$, and of the interface, respectively. Alternatively, accounting for (de)compression effects is possible with [43]

$$v_{3-i}(t) = \frac{dh_{3-i}}{dt} + \omega_{int}(t) h_{3-i}(t), \quad (13)$$

where ω_{int} is the velocity gradient evaluated at the interface z_{int} . In high-energy-density applications (including those involving blast waves and ablation) [41, 44], Eq. (13) would be used instead of Eq. (11).

The bubble and spike kinetic energies, kinetic energy dissipation rates, lengthscales, and mixing Reynolds numbers are

$$K_{3-i}(t) = \frac{v_{3-i}(t)^2}{2}, \quad \epsilon_{3-i}(t) = -F_d^{3-i}(t) v_{3-i}(t), \quad (14)$$

$$L_{3-i}(t) = C_L \frac{K_{3-i}(t)^{3/2}}{\epsilon_{3-i}(t)}, \quad Re_{3-i}(t) = \frac{v_{3-i}(t) h_{3-i}(t)}{\nu}$$

(if the kinematic viscosity $\nu \neq 0$), where C_L is a dimensionless coefficient. The bubble and spike kinetic energy equation is given by multiplying Eq. (1) by v_{3-i} :

$$\rho_{3-i} \frac{dK_{3-i}}{dt} = F_b^{3-i} v_{3-i} + F_s^{3-i} v_{3-i} + F_{vm}^{3-i} v_{3-i} + F_d^{3-i} v_{3-i} + F_{abl}^{3-i} v_{3-i}, \quad (15)$$

where the terms on the right side are the buoyancy production, shear production, virtual mass production, dissipation, and ablative destruction terms, respectively. The first, second, and fourth terms on the right side are analogous to those in the turbulent kinetic energy equation of a Reynolds-averaged turbulence model.

If the flow is accelerated by a shock, the acceleration in Eq. (2) is approximated by an impulse

$$g_{\text{eff}}(t) = \Delta v_s \delta(t), \quad (16)$$

where Δv_s is the velocity jump due to the shock passage through the interface. Integrating the buoyancy–drag equations with shocks can be difficult, in which case it is possible to set $C_d = 0$ and $dh_{3-i}/dt = 0$ in a shock, for example.

Other refinements of the model developed here are certainly possible (e.g., as suggested in Ref. [15]).

2.2. Analytical solutions for generic instability-induced mixing

Analytical solutions to the coupled nonlinear ordinary differential equations Eq. (1) can be obtained for the multimode case for incompressible Rayleigh–Taylor mixing with constant acceleration, impulsive Richtmyer–Meshkov mixing, and Kelvin–Helmholtz mixing under several approximations:

constant densities, late-time so that $E(t) \downarrow 0$, constant acceleration $g_{\text{eff}}(t) = g_0$ or impulsive acceleration (16), $\ell_i(t) \rightarrow h_i(t)$, and taking $\beta = 0$ and $n = 1$, such that Eqs. (2)–(6) simplify to

$$F_b^{3-i}(t) = C_b (\rho_1 - \rho_2) g_0, \quad (17)$$

$$F_s^{3-i}(t) = C_s \frac{\rho_i^2 \rho_{3-i}}{(\rho_i + \rho_{3-i})^2} \frac{(\Delta v)^2}{h_{3-i}(t) \delta_{i2} + h_i(t) \delta_{i1}}, \quad (18)$$

$$F_{vm}^{3-i}(t) = -C_{vm}^* \rho_i \frac{dv_{3-i}}{dt}, \quad (19)$$

$$F_d^{3-i}(t) = -\frac{C_d}{b} \frac{\rho_i |v_{3-i}(t)|}{h_{3-i}(t)} \sqrt{[R_i v_{3-i}(t)]^2 + (\Delta v)^2}, \quad (20)$$

$$F_{abl}^{3-i}(t) = -C_a \frac{\rho_i v_a |v_{3-i}(t)|}{h_{3-i}(t)}. \quad (21)$$

2.2.1. Analytical solution for constant acceleration Rayleigh–Taylor; impulsive Richtmyer–Meshkov, and Kelvin–Helmholtz mixing

Substituting the generic mixing layer width

$$h_i(t) = A_{h,i} t^{\theta_{h,i}}, \quad (22)$$

where the constant coefficients $A_{h,i}$ and exponents $\theta_{h,i}$ are specific to each instability, into Eq. (1) with Eqs. (17)–(21) gives

$$\begin{aligned} \mathcal{L} = & C_b (\rho_1 - \rho_2) g_0 \\ & + C_s \frac{\rho_i^2 \rho_{3-i}}{(\rho_i + \rho_{3-i})^2} \frac{(\Delta v)^2}{(A_{h,3-i} \delta_{i2} + A_{h,i} \delta_{i1}) t^{\theta_{h,i}}} \\ & - \frac{C_d}{b} \frac{\rho_i \theta_{h,3-i}}{t} \sqrt{(R_i \theta_{h,3-i} A_{h,3-i})^2 t^{2\theta_{h,i}-2} + (\Delta v)^2} \\ & - C_a \frac{\rho_i v_a \theta_{h,i}}{t} \end{aligned} \quad (23)$$

with $\mathcal{L} = \theta_{h,i} (\theta_{h,i} - 1) (\rho_{3-i} + C_{vm}^* \rho_i) A_{h,3-i} t^{\theta_{h,i}-2}$.

For Rayleigh–Taylor ($C_s = \Delta v = C_a = 0$), Richtmyer–Meshkov ($g_0 = C_s = \Delta v = C_a = 0$), and Kelvin–Helmholtz ($C_b = R_i = C_a = 0$) instability, the coefficients in the mixing layer widths and exponents are

$$A_{h,i} = \alpha_i A t g_0, \quad \theta_{h,i} = 2, \quad (24)$$

$$A_{h,i} = \left(\frac{\Delta v_s}{\theta_i h_{0,i}} \right)^{\theta_i}, \quad \theta_{h,i} = \theta_i, \quad (25)$$

$$A_{h,i} = \delta_i |\Delta v|, \quad \theta_{h,i} = 1, \quad (26)$$

respectively, with Atwood number $At = (\rho_1 - \rho_2)/(\rho_1 + \rho_2) > 0$. With these substitutions, Eq. (23) reduces to

$$\begin{aligned} 2(\rho_{3-i} + C_{vm}^* \rho_i) \alpha_{3-i} A t &= C_b (\rho_1 - \rho_2) \\ &\quad - \frac{4 C_d}{b} \rho_i \alpha_{3-i} A t \\ &\quad \times (R_i^n \delta_{i1} + R_i \delta_{i2}), \\ (\theta_{3-i} - 1)(\rho_{3-i} + C_{vm}^* \rho_i) &= -\frac{C_d}{b} \rho_i \theta_{3-i} R_i, \end{aligned}$$

$$0 = C_s \frac{\rho_i \rho_{3-i}}{(\rho_i + \rho_{3-i})^2} \frac{1}{\delta_{3-i} \delta_{i2} + \delta_i \delta_{i1}} - \frac{C_d}{b}$$

for each instability, and solving for α_{3-i} , θ_{3-i} , and δ_{3-i} gives

$$\alpha_{3-i}(C_b, C_d, C_{vm}^*) = \frac{C_b (\rho_{3-i} + \rho_i)}{2[\rho_{3-i} + (C_{vm}^* + \frac{2C_d}{b} R_i) \rho_i]}, \quad (27)$$

$$\theta_{3-i}(C_d, C_{vm}^*) = \frac{\rho_{3-i} + C_{vm}^* \rho_i}{\rho_{3-i} + (C_{vm}^* + \frac{C_d}{b} R_i) \rho_i}, \quad (28)$$

$$\delta_{3-i}(C_s, C_d) = \sqrt{\frac{b C_s}{C_d} \frac{\rho_i \rho_{3-i}}{(\rho_i + \rho_{3-i})^2}} \quad (29)$$

for the bubbles and spikes. It follows that the corresponding values for the total (bubble plus spike) mixing layer widths are

$$\begin{aligned} \alpha &= \alpha_i + \alpha_{3-i} \\ &= \frac{C_b (\rho_{3-i} + \rho_i)}{2[\rho_i + (C_{vm}^* + \frac{2C_d}{b} R_{3-i}) \rho_{3-i}]} \\ &\quad + \frac{C_b (\rho_{3-i} + \rho_i)}{2[\rho_{3-i} + (C_{vm}^* + \frac{2C_d}{b} R_i) \rho_i]}, \end{aligned} \quad (30)$$

$$\delta = \delta_i + \delta_{3-i} = 2 \sqrt{\frac{b C_s}{C_d} \frac{\rho_i \rho_{3-i}}{(\rho_i + \rho_{3-i})^2}}. \quad (31)$$

Note that the bubble and spike growth exponents for Richtmyer–Meshkov mixing are not additive. However, for very large times, $\theta \rightarrow \max(\theta_b, \theta_s) = \theta_s$.

These analytical solutions confirm that the model equations are consistent with the expected temporal scalings of mixing [i.e., Eqs. (24)–(26)] induced by the instabilities under consideration. In addition, the solutions provide relationships between growth parameters and exponents and the model coefficients (analogous to those obtained in self-similar analyses of Reynolds-averaged models) that can be used to calibrate the model as a function of Atwood number.

Using Eqs. (11), (20), and (22), Eqs. (14) become

$$K_{3-i}(t) = \frac{(\theta_{h,3-i} A_{h,3-i})^2 t^{2\theta_{h,3-i}-2}}{2}, \quad (32)$$

$$\begin{aligned} \epsilon_{3-i}(t) &= \frac{C_d}{b} \rho_i \theta_{h,3-i}^2 A_{h,3-i} t^{\theta_{h,3-i}-2} \\ &\quad \times \sqrt{(R_i \theta_{h,3-i} A_{h,3-i})^2 t^{2\theta_{h,3-i}-2} + (\Delta v)^2}, \end{aligned} \quad (33)$$

$$\begin{aligned} L_{3-i}(t) &= \frac{b C_L \theta_{h,3-i} (A_{h,3-i})^2}{2^{3/2} C_d \rho_{3-i}} t^{2\theta_{h,3-i}-1} \\ &\quad \times \frac{1}{\sqrt{(R_i \theta_{h,3-i} A_{h,3-i})^2 t^{2\theta_{h,3-i}-2} + (\Delta v)^2}}, \end{aligned} \quad (34)$$

$$Re_{3-i}(t) = \frac{\theta_{h,3-i} A_{h,3-i}^2 t^{2\theta_{h,3-i}-1}}{\nu} \quad (35)$$

for the bubble and spike, so that the total (bubble plus spike) values are given by the general expressions

$$K(t) = K_1(t) + K_2(t) = \frac{\theta_h^2 (A_{h,1} + A_{h,2})^2 t^{2\theta_h-2}}{2}, \quad (36)$$

$$\epsilon(t) = \epsilon_1(t) + \epsilon_2(t) = \frac{C_d}{b} \theta_h^2 t^{\theta_h-2} \quad (37)$$

$$\times \left[\rho_1 A_{h,2} \sqrt{(R_1 \theta_h A_{h,2})^2 t^{2\theta_h-2} + (\Delta v)^2} \right. \\ \left. + \rho_2 A_{h,1} \sqrt{(R_2 \theta_h A_{h,1})^2 t^{2\theta_h-2} + (\Delta v)^2} \right],$$

$$L(t) = L_1(t) + L_2(t) \quad (38)$$

$$= \frac{b C_L \theta_h}{2^{3/2} C_d} t^{2\theta_h-1}$$

$$\times \left[\frac{(A_{h,1})^2}{\rho_1 \sqrt{(R_2 \theta_h A_{h,1})^2 t^{2\theta_h-2} + (\Delta v)^2}} \right. \\ \left. + \frac{(A_{h,2})^2}{\rho_2 \sqrt{(R_1 \theta_h A_{h,2})^2 t^{2\theta_h-2} + (\Delta v)^2}} \right],$$

$$Re(t) = Re_1(t) + Re_2(t) = \frac{\theta_h (A_{h,1}^2 + A_{h,2}^2) t^{2\theta_h-1}}{\nu} \quad (39)$$

for Rayleigh–Taylor and Kelvin–Helmholtz mixing (and with more general expressions for Richtmyer–Meshkov mixing as $\theta_{3-i} \neq \theta_i$). These expressions provide the general temporal scalings of these quantities. Similar expressions can be obtained numerically for the more general model given by solving Eqs. (1)–(6). The value $C_L = 1$ will be assumed hereafter.

2.3. Model calibration using instability growth parameters and exponents

Two types of calibrations can be performed, appropriate for small and larger Atwood number cases. In the former case, symmetry between bubbles and spikes allows the calibrations to use the bubble (or spike) values of growth parameters and exponents. This choice has been utilized in calibrations of a K – L and K – L – a turbulence model using self-similar solutions obtained in the small Atwood number (i.e., Boussinesq) limit [52, 54]. In the latter case, the total values of the growth parameters and exponents are used instead as there is an asymmetry between the bubble and spike fronts. The expressions for the growth parameters and exponent provide three equations for four coefficients C_b , C_{vm}^* , C_d , and C_s ; a value of C_{vm}^* will be assumed below. Only the three-dimensional case is considered here, so that $b = 2/3$.

The calibration appropriate for finite Atwood number described above will be used here. With $R_i = 1$ and using $At = (\rho_s - \rho_b)/(\rho_s + \rho_b)$ and $\rho_s/\rho_b = (1 + At)/(1 - At)$, it fol-

lows that

$$\alpha(C_b, C_d, C_{vm}^*) = \frac{C_b (\rho_b + \rho_s)}{2 \left[\rho_b + \left(C_{vm}^* + \frac{2C_d}{b} \right) \rho_s \right]} \quad (40)$$

$$+ \frac{C_b (\rho_s + \rho_b)}{2 \left[\rho_s + \left(C_{vm}^* + \frac{2C_d}{b} \right) \rho_b \right]} \\ = \frac{C_b}{\left(\frac{1-At}{1+At} + C_{vm}^* + 2 \frac{C_d}{b} \right) (1 + At)} \\ + \frac{C_b}{\left(\frac{1+At}{1-At} + C_{vm}^* + 2 \frac{C_d}{b} \right) (1 - At)},$$

$$\theta(C_d, C_{vm}^*) = \frac{\rho_b + C_{vm}^* \rho_s}{\rho_b + \left(C_{vm}^* + \frac{C_d}{b} \right) \rho_s} = \frac{\frac{1+At}{1-At} + C_{vm}^*}{\frac{1+At}{1-At} + C_{vm}^* + \frac{C_d}{b}}, \quad (41)$$

$$\delta(C_s, C_d) = 2 \sqrt{\frac{b C_s}{C_d} \frac{\rho_b \rho_s}{(\rho_b + \rho_s)^2}} = \sqrt{\frac{b C_s}{C_d} (1 - At^2)}, \quad (42)$$

each of which is a function of Atwood number. Kelvin–Helmholtz growth decreases with increasing At , with the same dependence as in the linear growth rate. Solving these equations gives the analytic expressions for the model coefficients

$$C_b(\alpha, \theta) = \frac{\alpha [At(C_{vm}^* - 1) - C_{vm}^* - 1](\theta - 2)}{2\theta \{At[2 + C_{vm}^*(\theta - 2) - 3\theta] - (1 + C_{vm}^*)(\theta - 2)\}} \\ \times \left[At(4 - 6\theta) + At^2(C_{vm}^* - 1)(\theta - 2) - (1 + C_{vm}^*)(\theta - 2) \right], \quad (43)$$

$$C_d(\theta) = \frac{b(1 - \theta)[1 + C_{vm}^* + (1 - C_{vm}^*)At]}{\theta(1 - At)}, \quad (44)$$

$$C_s(\delta) = \frac{(1 - \theta)[1 - (C_{vm}^* - 1)At + C_{vm}^*] \delta^2}{\theta(1 - At^2)^2(1 + At)} \quad (45)$$

with $At \neq 1$. Note the strong dependence of C_b on At .

For example, taking (see Ref. [55])

$$\alpha = 0.05, \quad \theta = 0.30, \quad \delta = 0.07 \quad (46)$$

for Rayleigh–Taylor, Richtmyer–Meshkov [56, 57], and Kelvin–Helmholtz mixing [58, 59], respectively, gives the coefficients

$$C_b(C_{vm}^*, At) = \frac{0.1417 [At(C_{vm}^* - 1) - C_{vm}^* - 1]}{At(1.1 - 1.7 C_{vm}^*) + 1.7(1 + C_{vm}^*)} \quad (47)$$

$$\times \left[2.2 At - 1.7 At^2 (C_{vm}^* - 1) + 1.7(1 + C_{vm}^*) \right],$$

$$C_d(C_{vm}^*, At) = \frac{1.5556 [1 + C_{vm}^* + (1 - C_{vm}^*) At]}{1 - At}, \quad (48)$$

$$C_s(C_{vm}^*, At) = \frac{0.0114 [1 - (C_{vm}^* - 1) At + C_{vm}^*]}{(1 - At^2)^2 (1 + At)} \quad (49)$$

so that with $C_{vm}^* = 2$ (a different value could be chosen):

1. in the Boussinesq limit of small density contrast for $At = 0.05$,

$$C_b = 0.4364, \quad C_d = 4.8304, \quad C_s = 0.0356, \quad (50)$$

and;

2. for $At = 0.5$,

$$C_b = 0.5178, \quad C_d = 7.7778, \quad C_s = 0.0762. \quad (51)$$

The general expressions (47)–(49) will be used in the model applications below, where the full (rather than simplified) equations will be solved numerically. More generally, in a numerical computation, a time-dependent value of At could also be used rather than a constant value. Note that the calibrated coefficients obtained from self-similar solutions of Reynolds-averaged turbulence models are typically independent of Atwood number as a result of assuming $At \approx 0$ [52].

The buoyancy–drag–shear ordinary differential equations are solved here using the *Mathematica*[®] function `NDSolve` (with the `StiffnessSwitching` Method option for the Richtmyer–Meshkov case). *Mathematica*[®] is also used to construct and evolve the mean and turbulent fields.

2.4. Construction of turbulent diffusivity and viscosity

Using Eq. (22), a mixing layer turbulent diffusion coefficient is given dimensionally for each instability by the general expression

$$\begin{aligned} D_h(t) &= C_D h \frac{dh}{dt} \\ &= C_D \left(A_{h,3-i} t^{\theta_{h,3-i}} + A_{h,i} t^{\theta_{h,i}} \right) \\ &\quad \times \left(\theta_{h,3-i} A_{h,3-i} t^{\theta_{h,3-i}-1} + \theta_{h,i} A_{h,i} t^{\theta_{h,i}-1} \right), \end{aligned} \quad (52)$$

where C_D is a dimensionless coefficient. Note that Eq. (52) simplifies to

$$D_h(t) = C_D \theta_{h,i} (A_{h,3-i} + A_{h,i})^2 t^{2\theta_{h,i}-1} \quad (53)$$

for Rayleigh–Taylor and Kelvin–Helmholtz mixing. The corresponding mixing layer turbulent viscosity coefficient is $\nu_h(t) = Sc_t D_h(t)$, where Sc_t is the (constant) turbulent Schmidt number (assumed to be 0.7 here).

An alternative expression is inspired by the K – ϵ model [55–57] with K and ϵ given by Eqs. (36) and (37):

$$\begin{aligned} \nu_h(t) &= C_v \frac{K(t)^2}{\epsilon(t)} \\ &= \frac{C_v b \theta_h^2 (A_{h,1} + A_{h,2})^4 t^{3\theta_h-2}}{4 C_d} \\ &\quad \times \left[\rho_1 A_{h,2} \sqrt{(R_1 \theta_h A_{h,2})^2 t^{2\theta_h-2} + (\Delta v)^2} \right. \\ &\quad \left. + \rho_2 A_{h,1} \sqrt{(R_2 \theta_h A_{h,1})^2 t^{2\theta_h-2} + (\Delta v)^2} \right]^{-1} \\ &= Sc_t D_h(t). \end{aligned} \quad (54)$$

This expression will be used in the applications below with $C_v = 1$, $D_h \rightarrow D_t$, and $\nu_h \rightarrow \nu_t$.

Assuming an inverse parabolic profile, as used in self-similarity analysis of turbulence models [52, 54, 60, 61], a spatially-dependent turbulent diffusion coefficient can be constructed as a function of the form (z_{int} is the location of the initial interface separating the heavy and light fluids) [51]

$$\begin{aligned} D_t(z, t) &= D_h(t) \left[1 + \frac{z - z_{int}}{h_b(t)} \right] \left[1 - \frac{z - z_{int}}{h_s(t)} \right] \\ &\approx D_h(t) \left[1 - \frac{4(z - z_{int})^2}{h(t)^2} \right], \end{aligned} \quad (56)$$

and the last inverse parabolic expression follows if $h_b(t) \approx h_s(t)$ (i.e., if $At \ll 1$). Another possibility is a Gaussian function of the form

$$\begin{aligned} D_t(z, t) &= D_h(t) \exp \left[-\frac{(z - z_{int})^2}{h_b(t) h_s(t)} \right] \\ &\approx D_h(t) \exp \left[-\frac{4(z - z_{int})^2}{h(t)^2} \right] \end{aligned} \quad (57)$$

or a product of a parabolic and Gaussian function of the form

$$\begin{aligned} D_t(z, t) &= D_h(t) \left[1 + \frac{z - z_{int}}{h_b(t)} \right] \left[1 - \frac{z - z_{int}}{h_s(t)} \right] \\ &\quad \times \exp \left[-\frac{(z - z_{int})^2}{h_b(t) h_s(t)} \right] \\ &\approx D_h(t) \left[1 - \frac{4(z - z_{int})^2}{h(t)^2} \right] \exp \left[-\frac{4(z - z_{int})^2}{h(t)^2} \right]. \end{aligned} \quad (58)$$

The corresponding turbulent viscosity is

$$\nu_t(z, t) = Sc_t D_t(z, t). \quad (59)$$

The parabolic and parabolic–Gaussian forms have tails at the edges of the mixing layer, similar to those observed in experiments and numerical simulations. The profiles (56)–(58) have their maximum values at $z = z_{int}$. In the subsequent applications of the model, the form (58) will be assumed with $z_{int} = 0$.

2.5. Approximate analytic solutions for mean fields

It will be assumed that the light and heavy fluid occupy $z < z_{int}$ and $z > z_{int}$, where z_{int} is the interface position, and that the flows are incompressible. Reynolds- and Favre-averaged quantities, $\bar{\phi}$ and $\overline{\phi} = \overline{\rho\phi}/\bar{\rho}$, respectively, will be used below.

2.5.1. Rayleigh–Taylor and Richtmyer–Meshkov mixing

For Rayleigh–Taylor and Richtmyer–Meshkov mixing the mean heavy fluid mass fraction transport equation is the non-linear advection–diffusion equation

$$\begin{aligned} \bar{\rho} \left(\frac{\partial}{\partial t} + \bar{w} \frac{\partial}{\partial z} \right) \bar{m}_H &= \frac{\partial}{\partial z} \left(\bar{\rho} D \frac{\partial \bar{m}_H}{\partial z} - \overline{\rho m_H'' w''} \right) \\ &= \frac{\partial}{\partial z} \left[\bar{\rho} (D + D_t) \frac{\partial \bar{m}_H}{\partial z} \right] \end{aligned} \quad (60)$$

in the Fickian diffusion approximation (the mean light fluid mass fraction is $\bar{m}_L = 1 - \bar{m}_H$). A good approximation for the solution of this equation can be motivated as follows. In a

reference frame moving with the mean advection velocity \bar{w} , so that the advection term is zero, and with the Boussinesq approximation for the mean density, first note that the exact solution for $D_t = 0$ (molecular diffusion only) of the simplified equation

$$\frac{\partial \bar{m}_H}{\partial t} = \frac{\partial}{\partial z} \left[(D + D_t) \frac{\partial \bar{m}_H}{\partial z} \right] \quad (61)$$

is given by an error function [62]

$$\begin{aligned} \bar{m}_H(z, t) &= \frac{1}{2} \left\{ 1 + \operatorname{erf} \left[\frac{z - z_{int}}{\sqrt{D t}} \right] \right\} \\ &\approx \frac{1}{2} \left\{ 1 + \frac{2(z - z_{int})}{\sqrt{\pi} \sqrt{D t}} + \mathcal{O}(z^3) \right\}, \end{aligned} \quad (62)$$

(i.e., the error function is linear within the core of the mixing layer). Second, note that the solution consistent with Eq. (61) with $D = 0$ is a linear function [52, 54]

$$\bar{m}_H(z, t) = \frac{1}{2} \left[1 + \frac{2(z - z_{int})}{h(t)} \right] \approx \frac{1}{2} \left\{ 1 + \operatorname{erf} \left[\frac{2(z - z_{int})}{h(t)} \right] \right\} \quad (63)$$

(the $\sqrt{\pi}/2 \approx 0.87$ factor multiplying the error function is omitted to keep $\bar{m}_H \in [0, 1]$).

These observations inspire the approximate analytic form (where $h_0 = h_{0,b} + h_{0,s}$ and δ_0 is the initial diffuse interface width)

$$\bar{m}_H(z, t) = \frac{1}{2} \left\{ 1 + \operatorname{erf} \left[\frac{2(z - z_{int})}{\delta_0 + h_0 + h_{mix}(t)} \right] \right\} \quad (64)$$

with several possibilities for $h_{mix}(t)$:

$$h_{mix}(t) = \begin{cases} h(t) \\ \sqrt{2[D + D_t(t)]t} \\ \sqrt{2 \int_0^t [D + D_t(t')/C_D] dt'} \end{cases} . \quad (65)$$

The first choice corresponds to self-similar theory, where the similarity variable is

$$\eta = \frac{2z}{h(t)}, \quad (66)$$

and will be used in the applications below. The second choice can be regarded as the generalization of the molecular diffusion solution to include turbulent diffusion. Finally, the third choice arises from Eq. (52) with $D_h \rightarrow D_t$:

$$D_t(t) = C_D h \frac{dh}{dt} = C_D \frac{d}{dt} \left(\frac{h^2}{2} \right), \quad (67)$$

which can be integrated to obtain

$$h(t) = \sqrt{\frac{2}{C_D} \int_0^t D_t(t') dt'}. \quad (68)$$

The integral form of this expression utilizes the time-history of D_t , as compared to the second expression, which is local in time (but equivalent to the integral expression for simple power-law

time dependences of D_t). For example, using Eq. (53) in Eq. (68) it follows that

$$\begin{aligned} h(t) &= \sqrt{2 \theta_{h,i} (A_{h,3-i} + A_{h,i})^2 \int_0^t (t')^{2\theta_{h,i}-1} dt'} \\ &= (A_{h,3-i} + A_{h,i}) t^{\theta_{h,i}}, \end{aligned} \quad (69)$$

explicitly showing the consistency of these formulations.

Similarly, using the above approximations the mean density is

$$\bar{\rho}(z, t) = \rho_0 + \frac{\Delta\rho}{2} \operatorname{erf} \left[\frac{2(z - z_{int})}{\delta_0 + h_0 + h_{mix}(t)} \right], \quad (70)$$

where $\rho_0 = (\rho_b + \rho_s)/2$ and $\Delta\rho = \rho_s - \rho_b$. It is useful to briefly discuss how the width of the initial mass diffusion layer and molecular diffusivity affect the model predictions. These quantities affect the *growth rate* of the instability and can influence how rapidly the instability grows, becomes nonlinear, and eventually transitions to a fully turbulent state if a sufficiently large Reynolds number is achieved.

The initial diffusion layer width and diffusivity can influence the very early time evolution of the mean fields. From Eq. (64), it is seen from the denominator of the argument of the error function that the value of δ_0 will influence the very early time spreading of the mean mass fraction, i.e., the solution depends on δ_0 as long as its value is larger than $h_0 + h_{mix}(t)$; however, the flow becomes independent of the value of δ_0 once $h_0 + h_{mix}(t)$ exceeds δ_0 . From the second expression in Eq. (65), the value of the molecular diffusivity D can influence the very early time evolution of the mean mass fraction (and, hence, how early in time there is a transition to turbulence) as long as its value is less than the turbulent diffusivity D_t .

In a more general implementation of the model (for example, where the density variation cannot be neglected), Eq. (61) coupled to the mean density, momentum, internal (or total) energy, and any other Reynolds-averaged equations is solved numerically, as briefly discussed in Sec. 6. In problems with more than one interface, the buoyancy–drag–shear equations can be solved at each interface with local input data.

2.5.2. Kelvin–Helmholtz mixing

For Kelvin–Helmholtz mixing, the mean shear velocity transport equation is

$$\begin{aligned} \bar{\rho} \left(\frac{\partial}{\partial t} + \bar{w} \frac{\partial}{\partial z} \right) \bar{v} &= \frac{\partial}{\partial z} \left(\mu \frac{\partial \bar{v}}{\partial z} - \overline{\rho v' w'} \right) \\ &= \frac{\partial}{\partial z} \left[(\mu + \mu_t) \frac{\partial \bar{v}}{\partial z} \right]. \end{aligned} \quad (71)$$

Using the arguments propounded in Sec. 2.5.1 above for Rayleigh–Taylor and Richtmyer–Meshkov mixing, the simplified form of this equation

$$\frac{\partial \bar{v}}{\partial t} = \frac{\partial}{\partial z} \left[(v + v_t) \frac{\partial \bar{v}}{\partial z} \right] \quad (72)$$

has an approximate analytic solution

$$\bar{v}(z, t) = v_0 \left\{ 1 + At_v \operatorname{erf} \left[\frac{2(z - z_{int})}{\delta_0 + h_0 + h_{mix}(t)} \right] \right\}, \quad (73)$$

where $v_0 = (v_s + v_b)/2$ is the average stream velocity and $At_v = (v_s - v_b)/(v_b + v_s)$ is the ‘velocity Atwood number’ in analogy with the usual density Atwood number. There are several possibilities for $h_{mix}(t)$:

$$h_{mix}(t) = \begin{cases} h(t) \\ \sqrt{2} [v + v_t(t)] t \\ \sqrt{2} \int_0^t [v + v_t(t')] dt' \end{cases} \quad (74)$$

with $v_t(t) = Sc_t D_t(t)$. Note that in shear-driven mixing there are no ‘bubbles’ or ‘spikes’; however, the notation is retained here for consistency with the previously discussed cases.

As in the case of Rayleigh–Taylor and Richtmyer–Meshkov mixing, the initial diffusion layer width and viscosity can influence the very early time evolution of the mean fields. From Eq. (73), it is seen from the denominator of the argument of the error function that the value of δ_0 will influence the very early time spreading of the mean shear velocity, i.e., the solution depends on δ_0 as long as its value is larger than $h_0 + h_{mix}(t)$; however, the flow becomes independent of the value of δ_0 once $h_0 + h_{mix}(t)$ exceeds δ_0 . From the second expression in Eq. (74), the value of the molecular viscosity ν can influence the very early time evolution of the mean mass fraction (and, hence, how early in time there is a transition to turbulence) as long as its value is less than the turbulent viscosity ν_t .

More generally, Eq. (71) coupled to other Reynolds-averaged equations can be solved numerically, as briefly discussed in Sec. 6.

3. Application to Rayleigh–Taylor mixing

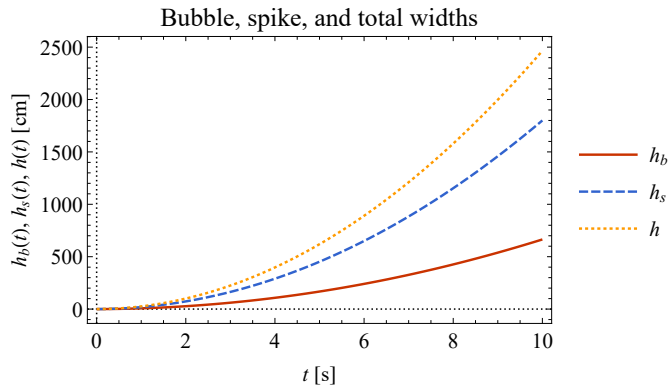


Figure 1: Time-evolution of the bubble, spike, and total mixing layer widths given by Eqs. (22) and (24) for Rayleigh–Taylor mixing.

Let $g_{eff} = g_0 = 981 \text{ cm/s}^2$, $\rho_b = 1 \text{ g/cm}^3$, $\rho_s = 3 \text{ g/cm}^3$, $At = 0.5$, $\nu = D = 0.01 \text{ cm}^2/\text{s}$, $\delta_0 = 0.1 \text{ cm}$, $h_{0,b} = h_{0,s} = 0.01 \text{ cm}$, $v_{0,b} = v_{0,s} = 0$, and $z_{int} = 0$. The final time is $t_f = 10 \text{ s}$. This case is an adaptation of the Rayleigh–Taylor mixing case considered in Ref. [55].

Figure 1 shows the time-evolution of the bubble, spike, and total mixing layer widths, and Fig. 2 shows the corresponding values of the growth parameters $\alpha_{b,s}(t) = h_{b,s}(t)/(Atg_0 t^2)$. The

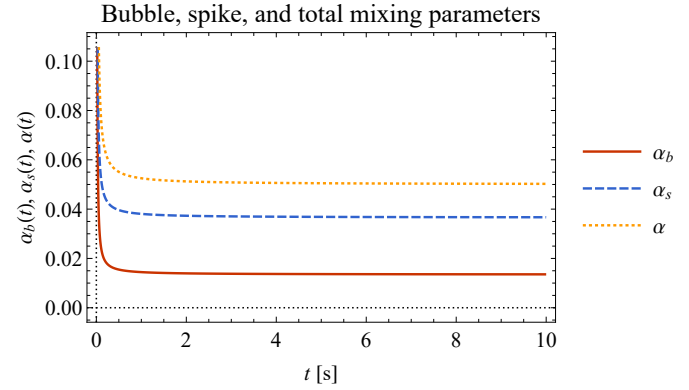


Figure 2: Time-evolution of the bubble, spike, and total mixing layer growth parameters given by Eqs. (36)–(39) together with Eq. (24) for Rayleigh–Taylor mixing.

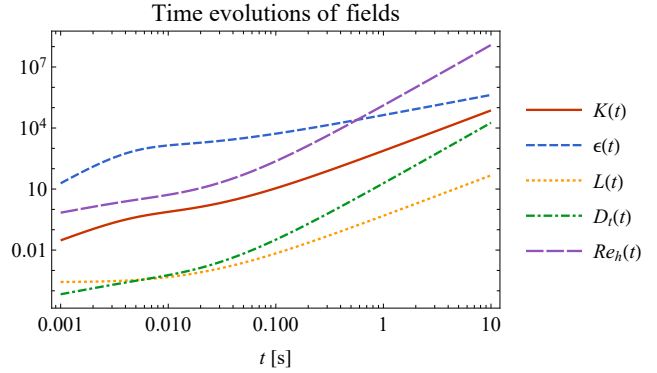


Figure 3: Time-evolution of the turbulent kinetic energy, kinetic energy dissipation rate, lengthscale, diffusivity, and mixing Reynolds number for Rayleigh–Taylor mixing.

widths grow quadratically in time, as expected for self-similar Rayleigh–Taylor mixing. Constant (asymptotic) values of α_b and α_s are attained rapidly following a short transient, with the value of α in agreement with the calibration. At the final time $\alpha_b = 0.014$ and $\alpha_s = 0.037$, and $\alpha_s/\alpha_b = 2.71$.

Figure 3 shows the time-evolution of the turbulent kinetic energy, kinetic energy dissipation rate, lengthscale, diffusivity, and mixing Reynolds number (36)–(39) on a log-log scale. Transient growth is observed at early times, transitioning to the expected power-laws growths for $t > 0.3 \text{ s}$.

Figures 4–7 show the spatiotemporal evolution of the turbulent kinetic energy, kinetic energy dissipation rate, lengthscale, and diffusivity, as constructed using the procedure described in Sec. 2.4. The peak values of the fields grow with the expected t^2 , t , t^2 , and t^3 power-laws, respectively. At early times, the profiles are a maximum near the interface $z_{int} = 0$ and exhibit increasing asymmetry toward the light (bubble) side as time evolves. The locations of the peak values also shift towards the bubble side at an increasing rate.

Figures 8 and 9 show the spatiotemporal evolution of the mean heavy mass fraction and density given by Eqs. (64) and

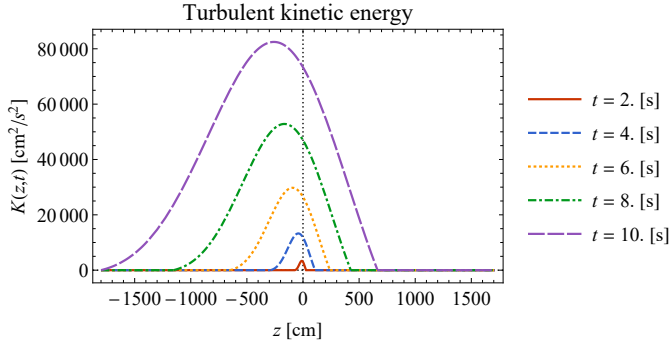


Figure 4: Spatiotemporal evolution of the turbulent kinetic energy (36) for Rayleigh–Taylor mixing.

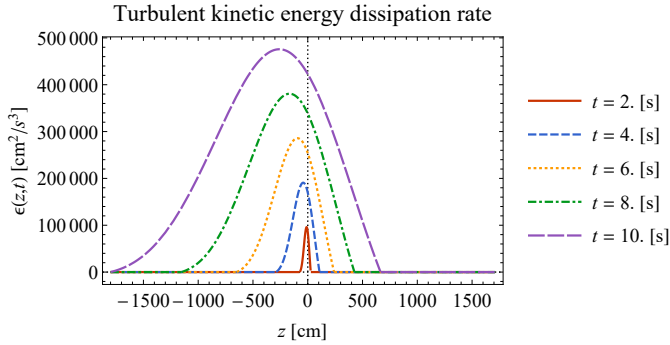


Figure 5: Spatiotemporal evolution of the turbulent kinetic energy dissipation rate (37) for Rayleigh–Taylor mixing.

(70). The initial values are slightly diffused step functions, with the profiles widening and becoming less steep as the mixing progresses. These profiles are much more symmetric about the interface than the turbulent fields. Both profiles are nearly linear within the core of the mixing layer $-h(t)/3 \lesssim z \lesssim h(t)/3$.

4. Application to reshocked Richtmyer–Meshkov mixing

With the same approximation used in Sec. 3 above, Eqs. (61)–(70) are formally the same for Richtmyer–Meshkov mixing. Consider an air/sulfur hexafluoride case with $\Delta v_s = 981$ cm/s², $\Delta v_r = 1.2\Delta v_s$ at $t_{res} = 5$ s, $\rho_b = 1.225 \times 10^{-3}$ g/cm³, $\rho_s = 6.164 \times 10^{-3}$ g/cm³, $At = 0.67$, $D = 0.151$ cm²/s (the average value of a 50%/50% mixture of air and SF₆), $\delta_0 = 0.1$ cm, $h_{0,b} = h_{0,s} = 0.01$ cm, $v_{0,b} = v_{0,s} = \Delta v_s$, and $z_{int} = 0$. The acceleration representing the initial and second shock is taken as

$$g_{\text{eff}}(t) = \begin{cases} \Delta v_s \exp(-1000 t^2) & \text{if } t < t_{res} \\ \Delta v_r \exp[-1000 (t - t_{res})^2] & \text{if } t \geq t_{res} \end{cases}, \quad (75)$$

where the exponential factors make the acceleration zero for times between the first and second shocks, and are thus effectively delta functions at $t = 0$ and $t = t_{res}$. The final time is $t_f = 10$ s.

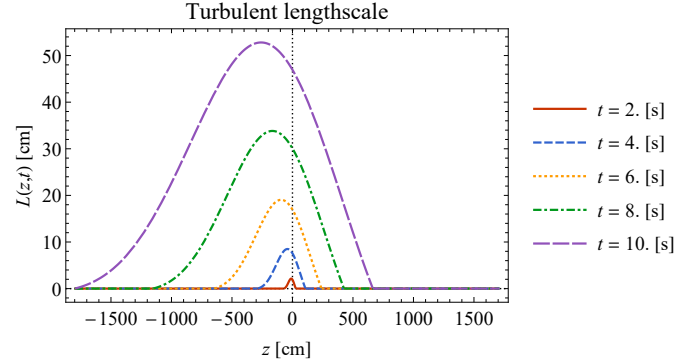


Figure 6: Spatiotemporal evolution of the turbulent lengthscale (38) for Rayleigh–Taylor mixing.

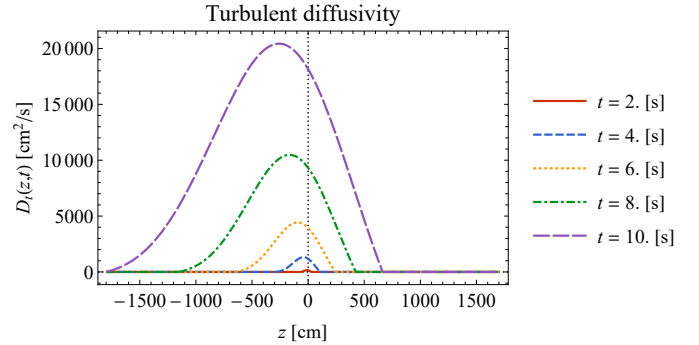


Figure 7: Spatiotemporal evolution of the turbulent diffusivity (58) for Rayleigh–Taylor mixing.

Figure 10 shows the time-evolution of the bubble, spike, and total mixing layer widths. The widths evolve with the same power-laws given by Eqs. (22) and (25) before and after reshock. This width is similar to that phenomenologically proposed by Mikaelian [63]. Figure 11 shows the time-evolution of the bubble and spike growth exponents up to the time of reshock. These values are obtained by solving the transcendental equations

$$h_{b,s}(t) = \left(\frac{\Delta v_s t}{\theta_{b,s} h_{0,b,s}} \right)^{\theta_{b,s}} \quad (76)$$

for the exponents at each time before reshock. At the time of reshock, $\theta_b = 0.17$ and $\theta_s = 0.34$, with $\theta_s/\theta_b = 2.0$, and at the final time after reshock, $\theta_b = 0.24$ and $\theta_s = 0.44$, with $\theta_s/\theta_b = 1.8$. The bubble width is significantly smaller than the spike width. Both θ_b and θ_s are slowly decreasing with time: when the layer is evolved much longer in time and without reshock, the numerical value of the spike (and total) exponent agrees closely with the calibration value.

Figure 12 shows the time-evolution of the turbulent kinetic energy, kinetic energy dissipation rate, lengthscale, diffusivity, and mixing Reynolds number (36)–(39) on a log-log scale. Transient growth is observed at early times, transitioning to the expected power-laws decays for $t > 0.014$ s following passage of the initial shock. At reshock, there is a strong amplification

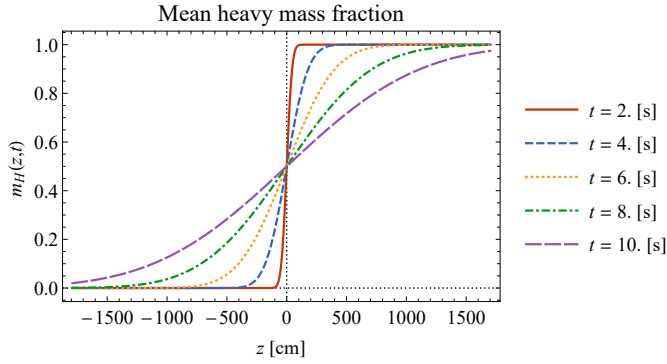


Figure 8: Spatiotemporal evolution of the mean heavy mass fraction (64) for Rayleigh–Taylor mixing.

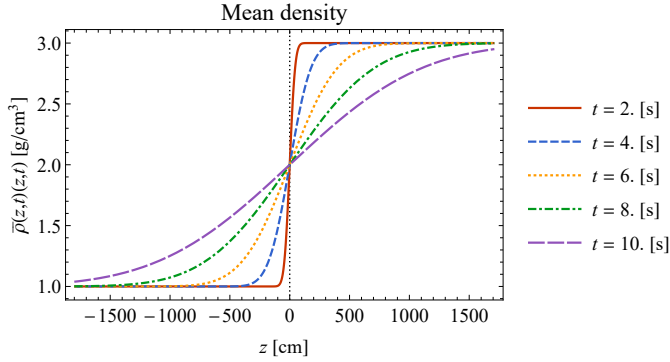


Figure 9: Spatiotemporal evolution of the mean density (70) for Rayleigh–Taylor mixing.

of the fields as expected, after which the expected power-law decays are evident (except for the lengthscale, which continues to grow).

Figures 13–16 show the spatiotemporal evolution of the turbulent kinetic energy, kinetic energy dissipation rate, lengthscale, and diffusivity, as constructed using the procedure described in Sec. 2.4. Before reshock, the peak values of the turbulent kinetic and its dissipation rate decrease with the expected $t^{2\theta-2}$ and $t^{2\theta-3}$ power-laws (not seen on the scale of the plots), while the peak values of the turbulent lengthscale and viscosity grow with the expected t^θ and $t^{2\theta-1}$ power-laws. Reshock then amplifies all of the fields instantaneously, after which they decrease as the flow is in a decaying state. At early times, the profiles are a maximum near the interface $z_{int} = 0$ and exhibit increasing asymmetry toward the light (bubble) side as time evolves (as in Rayleigh–Taylor mixing).

Figures 17 and 18 show the spatiotemporal evolution of the mean heavy mass fraction and density given by Eqs. (64) and (70). Before reshock, the profiles slowly widen as the mixing layer grows, with the widening significantly enhanced following reshock when the layer grows much more rapidly due to the additional energy imparted into the evolving layer by the second shock (or impulse).

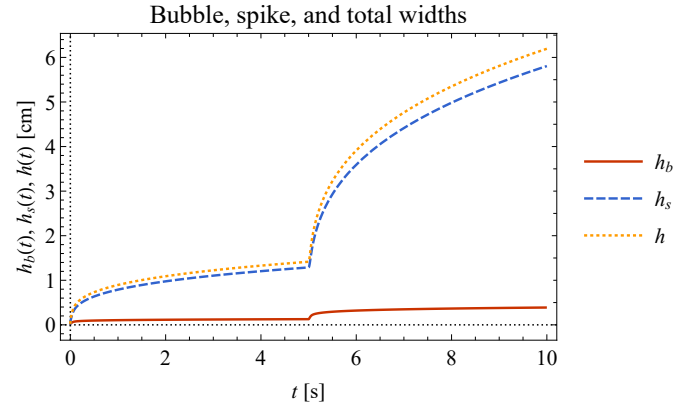


Figure 10: Time-evolution of the bubble, spike, and total mixing layer widths given by Eqs. (22) and (25) for reshocked Richtmyer–Meshkov mixing.

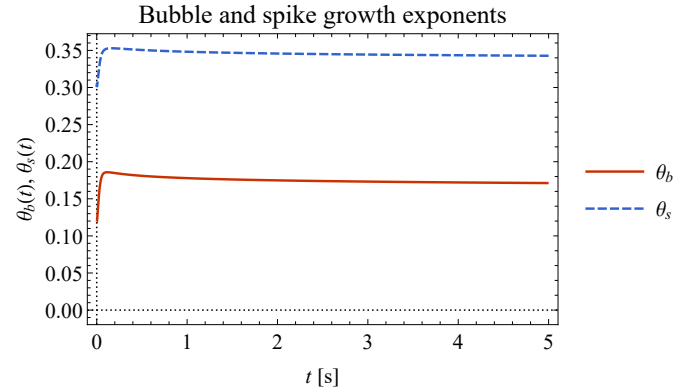


Figure 11: Time-evolution of the bubble and spike mixing layer growth exponents up to t_r for reshocked Richtmyer–Meshkov mixing.

5. Application to Kelvin–Helmholtz mixing

Let $g_{\text{eff}} = 0$, $v_b = 920$ cm/s, $v_s = 140$ cm/s, $\Delta v = v_b - v_s = 780$ cm/s, $\rho_b = 1.664 \times 10^{-4}$ g/cm³, $\rho_s = 1.165 \times 10^{-3}$ g/cm³, $At = 0.75$, $\nu = 0.01$ cm²/s, $\delta_0 = 0.1$ cm, $h_{0,b} = h_{0,s} = 0.01$ cm, $v_{0,b} = v_{0,s} = 0$, and $z_{int} = 0$. The final time is $t_f = 2$ s. This case corresponds to the nitrogen/helium Kelvin–Helmholtz mixing case considered in Ref. [64].

Figure 19 shows the time-evolution of the bubble, spike, and total mixing layer widths, and Fig. 20 shows the corresponding values of the growth parameters $\delta_{b,s}(t) = h_{b,s}(t)/(\Delta vt)$. The widths grow linearly in time, as expected for self-similar Kelvin–Helmholtz mixing, with the bubble width growing slightly faster than the spike width. Constant (asymptotic) values of $\delta_b = 0.038$ and $\delta_s = 0.033$ are attained rapidly, with the value of δ in agreement with the calibration. For this finite Atwood number case, there is a slight asymmetry between the bubble and spike fronts.

Figure 21 shows the time-evolution of the turbulent kinetic energy, kinetic energy dissipation rate, lengthscale, viscosity, and mixing Reynolds number (36)–(39) on a log-log scale. Unlike in the Rayleigh–Taylor and Richtmyer–Meshkov cases,

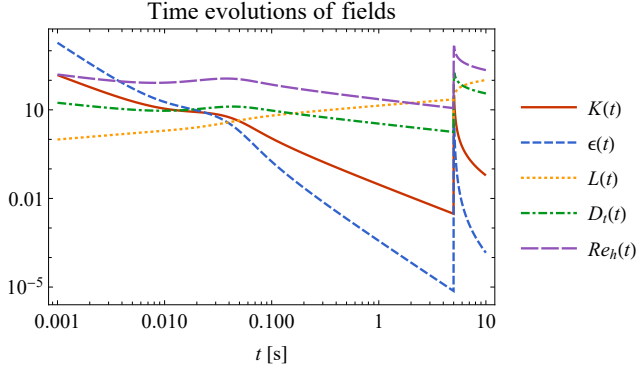


Figure 12: Time-evolution of the turbulent kinetic energy, kinetic energy dissipation rate, lengthscale, diffusivity, and mixing Reynolds number given by Eqs. (36)–(39) together with Eq. (25) for reshocked Richtmyer–Meshkov mixing.

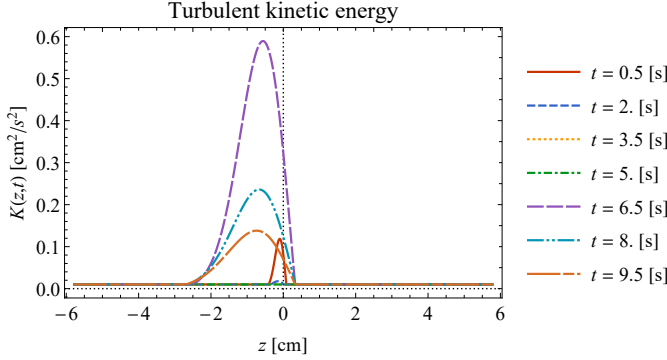


Figure 13: Spatiotemporal evolution of the turbulent kinetic energy (36) for reshocked Richtmyer–Meshkov mixing.

transient growth is not observed at early times. The lengthscale, viscosity, and Reynolds number grow with the expected power laws, the dissipation rate decreases with the expected power-law, and the kinetic energy remains constant.

Figures 22–25 show the spatiotemporal evolution of the turbulent kinetic energy, kinetic energy dissipation rate, lengthscale, and viscosity, as constructed using the procedure described in Sec. 2.4. The peak values of the fields grow with the expected t^0 , t^{-1} , t , and t power-laws, respectively. The profiles are slightly asymmetric about $z_{int} = 0$ as $At > 0$. The turbulent kinetic energy profile broadens with time, but the peak value remains constant.

Figure 26 shows the spatiotemporal evolution of the mean shear velocity given by Eq. (73). The profile evolves from a slightly diffuse step function at the initial time to wider profiles with a decreasing gradient (analogous to the mean density in Rayleigh–Taylor mixing). Note that the profile is nearly linear within the core of the layer. The self-similar mean shear velocity is linear in the self-similar variable (66) [55, 61]. Figure 27 shows the spatiotemporal evolution of the mean density given by Eq. (70). The profiles slowly widen as the mixing layer grows and become nearly linear at the latest time.

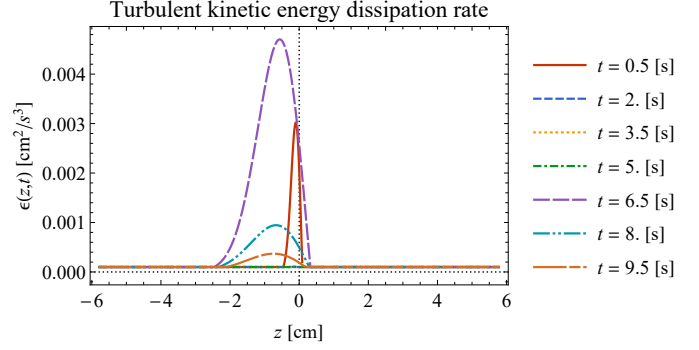


Figure 14: Spatiotemporal evolution of the turbulent kinetic energy dissipation rate (37) for reshocked Richtmyer–Meshkov mixing.

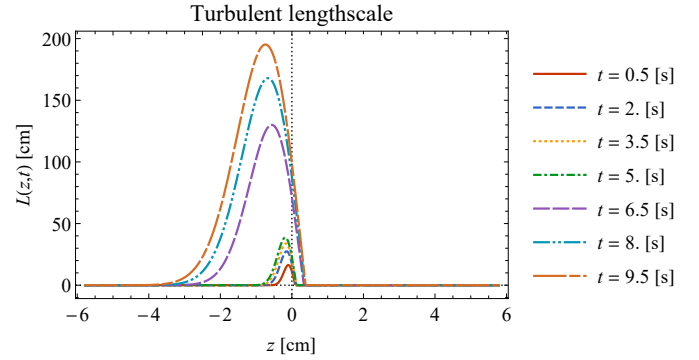


Figure 15: Spatiotemporal evolution of the turbulent lengthscale (38) for reshocked Richtmyer–Meshkov mixing.

6. Remarks on applications to more general flows

The model proposed here was applied as a proof-of-principle to pure Rayleigh–Taylor, reshocked Richtmyer–Meshkov, and Kelvin–Helmholtz mixing in Secs. 3–5 to demonstrate its utility. The application of the model to more general flows driven by hydrodynamic instabilities such as those encountered in astrophysics is briefly outlined here. Potential applications of this model include supernova explosions and molecular cloud dynamics, in which all three instabilities coexist.

The general hydrodynamic equations describe the conservation of mass, momentum, total (or internal) energy, and species mass fractions. The multicomponent Reynolds-averaged forms of these equations [56, 57]

$$\frac{\partial \bar{\rho}}{\partial t} + \frac{\partial}{\partial x_j} (\bar{\rho} \bar{v}_j) = 0, \quad (77)$$

$$\frac{\partial}{\partial t} (\bar{\rho} \bar{v}_i) + \frac{\partial}{\partial x_j} (\bar{\rho} \bar{v}_i \bar{v}_j) = \bar{\rho} g_i - \frac{\partial \bar{p}}{\partial x_i} + \frac{\partial \bar{\sigma}_{ij}}{\partial x_j} - \frac{\partial \tau_{ij}}{\partial x_j}, \quad (78)$$

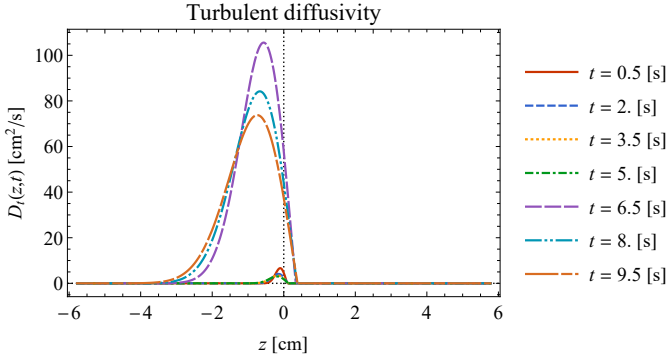


Figure 16: Spatiotemporal evolution of the turbulent diffusivity (58) for reshocked Richtmyer–Meshkov mixing.

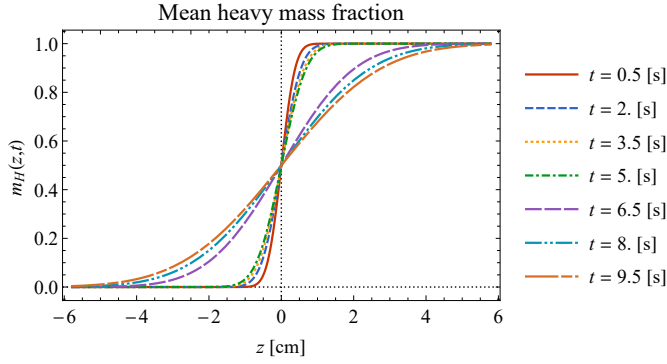


Figure 17: Spatiotemporal evolution of the mean heavy mass fraction (64) for reshocked Richtmyer–Meshkov mixing.

$$\begin{aligned} \frac{\partial}{\partial t}(\bar{\rho}\bar{e}) + \frac{\partial}{\partial x_j}(\bar{\rho}\bar{e}\bar{v}_j) &= \bar{\rho}g_j\bar{v}_j - \frac{\partial}{\partial x_j}(\bar{p}\bar{v}_j + \bar{p}\bar{v}_j'') \\ &\quad - \frac{\partial}{\partial x_j}(\bar{\tau}_{ij}\bar{v}_i'') + \frac{\partial}{\partial x_j}(\bar{\sigma}_{ij}\bar{v}_i'') \\ &\quad + \frac{\partial}{\partial x_j}\left[(\bar{\kappa} + \kappa_t)\frac{\partial\bar{T}}{\partial x_j} + \frac{\mu_t}{\sigma_U}\frac{\partial\bar{U}}{\partial x_j}\right] \\ &\quad + \frac{\partial}{\partial x_j}\left[\left(\bar{\mu} + \frac{\mu_t}{\sigma_K}\right)\frac{\partial K}{\partial x_j}\right] + \frac{\partial\bar{H}_j}{\partial x_j}, \end{aligned} \quad (79)$$

$$\frac{\partial}{\partial t}(\bar{\rho}\bar{m}_r) + \frac{\partial}{\partial x_j}(\bar{\rho}\bar{m}_r\bar{v}_j) = \bar{R}_r - \frac{\partial\bar{J}_{r,j}}{\partial x_j} + \frac{\partial}{\partial x_j}\left(\frac{\mu_t}{\sigma_m}\frac{\partial\bar{m}_r}{\partial x_j}\right), \quad (80)$$

have been closed using gradient-diffusion closures, where $\bar{\sigma}_{ij} = 2\bar{\mu}S_{ij}^*$ is the mean viscous stress tensor,

$$\tau_{ij} = \overline{\rho v_i'' v_j''} = \frac{2}{3}\bar{\rho}K\delta_{ij} - 2\mu_t\bar{S}_{ij}^* \quad (81)$$

is the Reynolds stress tensor (in the Boussinesq approximation), $\bar{S}_{ij}^* = (1/2)[\partial\bar{v}_i/\partial x_j + \partial\bar{v}_j/\partial x_i - (2/3)\delta_{ij}\partial\bar{v}_k/\partial x_k]$ is the traceless mean strain-rate tensor,

$$\bar{v}_i'' = \frac{\nu_t}{\sigma_\rho\bar{\rho}}\left(\frac{\partial\bar{\rho}}{\partial x_i} - \frac{\bar{\rho}}{\bar{\gamma}\bar{p}}\frac{\partial\bar{p}}{\partial x_i}\right) \quad (82)$$

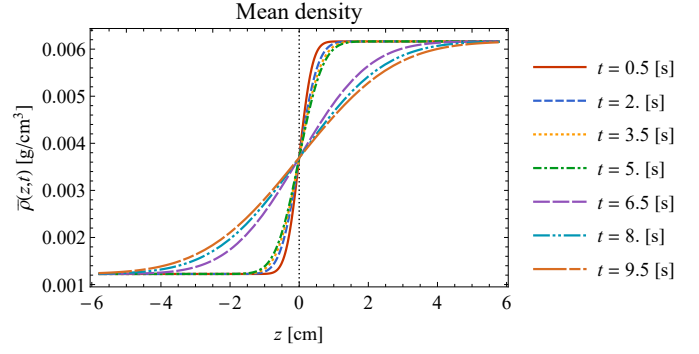


Figure 18: Spatiotemporal evolution of the mean density (70) for reshocked Richtmyer–Meshkov mixing.

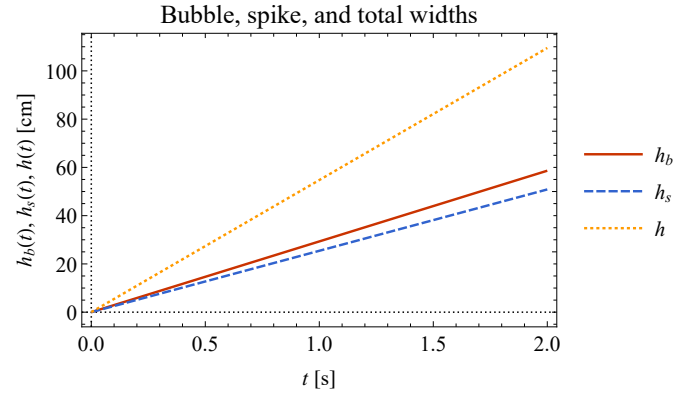


Figure 19: Time-evolution of the bubble, spike, and total mixing layer widths given by Eqs. (22) and (26) for Kelvin–Helmholtz mixing.

is the averaged Favre fluctuating velocity (or mass flux velocity), $\bar{e} = \bar{v}^2/2 + K + \bar{U}$ is the mean total energy, $\bar{U} = \bar{p}/[(\bar{\gamma} - 1)\bar{\rho}]$ is the mean internal energy (for an ideal gas with mixture adiabatic exponent $\bar{\gamma}$), $\bar{\kappa} = \bar{\rho}c_p\bar{\chi}$ is the mean thermal conductivity, r labels the species,

$$\bar{J}_{r,j} = -\bar{\rho}\left(\bar{D}_r\frac{\partial\bar{m}_r}{\partial x_j} - \bar{m}_r\sum_s\bar{D}_s\frac{\partial\bar{m}_s}{\partial x_j}\right), \quad (83)$$

$$\bar{H}_j = -\sum_r\bar{h}_r\bar{J}_{r,j} + \bar{\rho}D_t\sum_r\bar{h}_r\frac{\partial\bar{m}_r}{\partial x_j}, \quad (84)$$

\bar{D}_r is the mean molecular diffusivity of fluid r , $\bar{h}_r = \bar{U}_r + \bar{p}_r/\bar{\rho}_r$ is the mean enthalpy of fluid r , and \bar{R}_r is the mean (e.g., thermonuclear) reaction rate of fluid r . The turbulent viscosity, diffusivity, and conductivity are

$$\nu_t = \frac{\mu_t}{\bar{\rho}} = C_\nu\frac{K^2}{\epsilon}, \quad D_t = \frac{\nu_t}{Sc_t}, \quad \kappa_t = \frac{\bar{\rho}c_p\nu_t}{Pr_t}. \quad (85)$$

Equations (77)–(80) are solved numerically (with given values of the turbulent Schmidt and Prandtl numbers, Sc_t and Pr_t , in conjunction with the buoyancy–shear–drag equations at each interface, with the bubble and spike widths used to construct the turbulent diffusivity, viscosity, and conductivity needed for

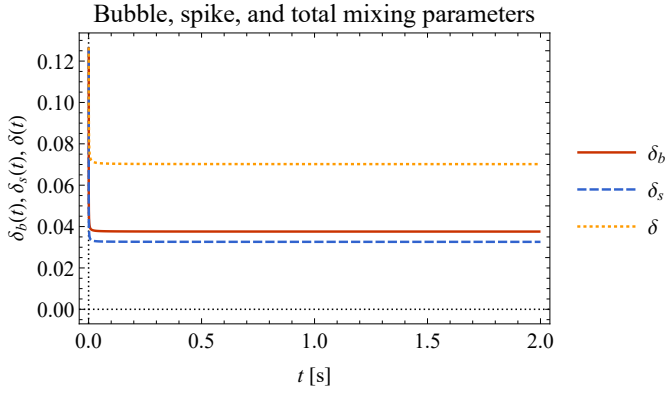


Figure 20: Time-evolution of the bubble, spike, and total mixing layer growth parameters for Kelvin–Helmholtz mixing.

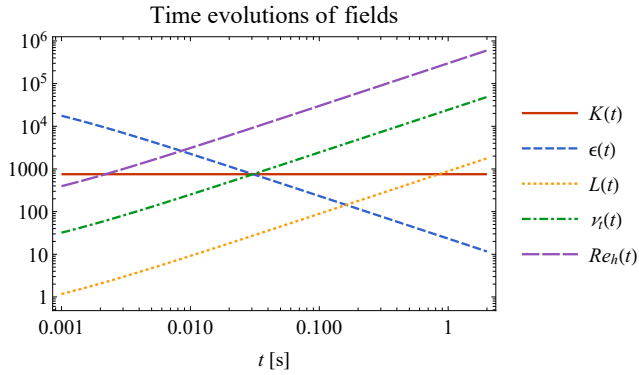


Figure 21: Time-evolution of the turbulent kinetic energy, kinetic energy dissipation rate, lengthscale, viscosity, and mixing Reynolds number given by Eqs. (36)–(39) together with Eq. (26) for Kelvin–Helmholtz mixing.

the gradient-diffusion closures. No modeled turbulent transport equations are needed.

7. Summary and conclusions

The theoretical model proposed and demonstrated here for binary mixing is based on the observation that the mean field evolution is fundamentally determined by a turbulent diffusivity and viscosity (as assumed in the original mixing-length turbulence models) if gradient-diffusion models are used to close the turbulent fluxes in the mean transport equations, i.e., equations for the turbulent kinetic energy and another quantity (turbulent kinetic energy dissipation rate or lengthscale) are not essential. The model equations combine elements of previously developed buoyancy–drag models, and also incorporate shear in a unified manner. This model can thus be regarded as intermediate between a buoyancy–drag model and a Reynolds-averaged transport model.

The buoyancy–shear–drag equations for the bubble and spike were first solved analytically for simplified configurations corresponding to each instability (for which the equations admit scale-similar solutions) to obtain the relations between the

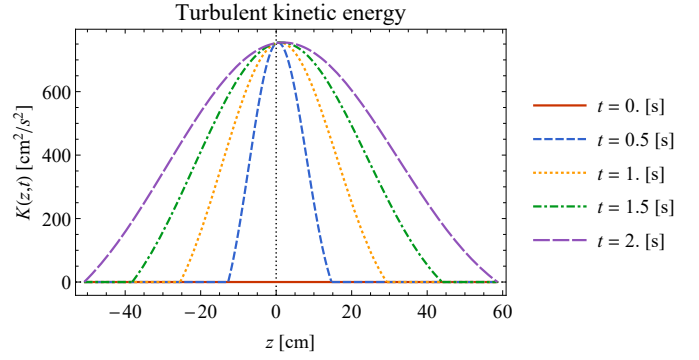


Figure 22: Spatiotemporal evolution of the turbulent kinetic energy (36) for Kelvin–Helmholtz mixing.

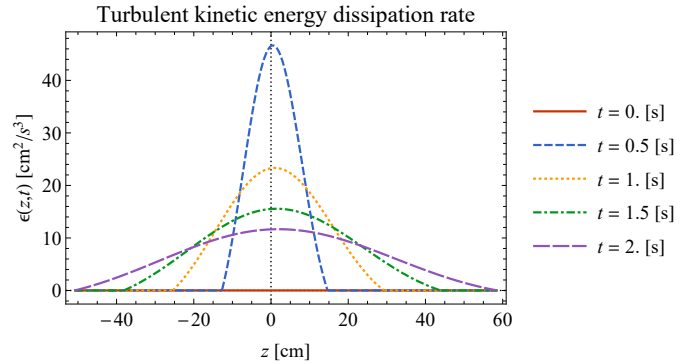


Figure 23: Spatiotemporal evolution of the turbulent kinetic energy dissipation rate (37) for Kelvin–Helmholtz mixing.

model coefficients and observables (i.e., the instability growth parameters and exponents α , θ , and δ); these relations were inverted to obtain the model coefficients as functions of the observables, Atwood number, and virtual mass coefficient. Using specific values of the observables, the equations of the calibrated model were then solved numerically for the bubble and spike mixing layer widths for representative mixing cases corresponding to each instability to obtain the time-dependent turbulent diffusivity or viscosity. These quantities were converted to spatial fields by multiplying their time-dependent values by an assumed space–time profile motivated by self-similarity; the resulting expressions were then used to solve the mean flow equations numerically in conjunction with other Reynolds-averaged equations. The calibration method is analogous to that used in the self-similar approximation of Reynolds-averaged turbulence models.

To demonstrate the application of the model, the numerically obtained time-dependent turbulent diffusivity and viscosity were used to evolve the mean heavy mass fraction for Rayleigh–Taylor and reshocked Richtmyer–Meshkov mixing and mean shear velocity for Kelvin–Helmholtz mixing in space and time using approximate analytic solutions to the pertinent mean flow equations inspired by self-similarity theory. Specifically, in a reference frame moving with the mean velocity (such

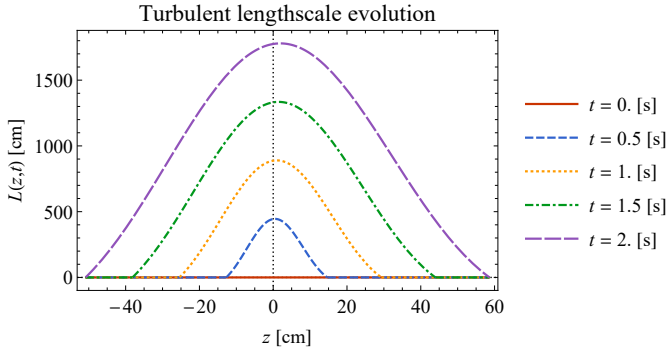


Figure 24: Spatiotemporal evolution of the turbulent lengthscale Eq. (38) for Kelvin–Helmholtz mixing.

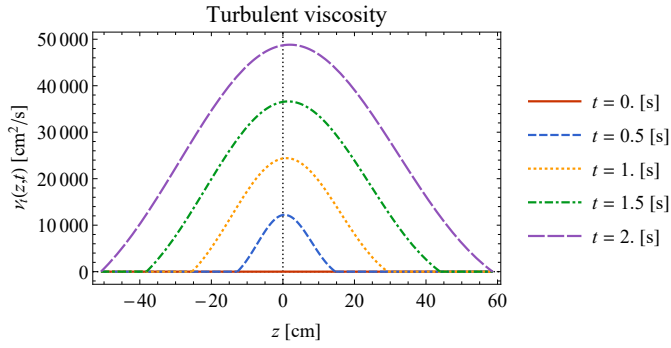


Figure 25: Spatiotemporal evolution of the turbulent viscosity Eq. (59) for Kelvin–Helmholtz mixing.

that the mean advection terms vanish), the mean flow equations reduce to diffusion equations with approximate analytical solutions given by error function profiles: these solutions can be regarded as extensions of the well-known molecular diffusion solutions to the turbulent case.

It was shown that the numerical solutions of the model calibrated using specific values of the instability growth parameters and exponents:

1. produces mixing layer widths in agreement with the expected self-similar growth power laws in time;
2. gives spatiotemporal profiles of turbulent fields (kinetic energy, kinetic energy dissipation rate, lengthscale, diffusivity, and viscosity) that are both expected and consistent with previous results, including the asymmetry between bubbles and spikes;
3. predicts the expected power-law growths and decays of the spatially-integrated turbulent fields, and;
4. gives spatiotemporal profiles of the mean fields that are both expected and consistent with previous results.

For reshocked Richtmyer–Meshkov mixing, it was shown that the model reproduces the rapid growth of turbulence and mixing induced by the second shock interaction with the evolving bubble and spike side layers. The more general application of the model to other hydrodynamic instability-driven turbulent flows was discussed.

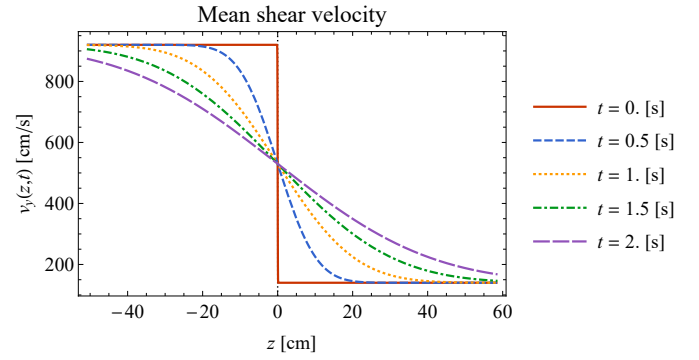


Figure 26: Spatiotemporal evolution of the mean shear velocity Eq. (73) for Kelvin–Helmholtz mixing.

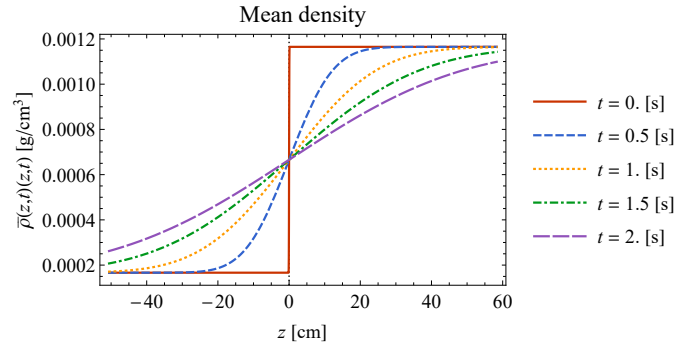


Figure 27: Spatiotemporal evolution of the mean density (70) for Kelvin–Helmholtz mixing.

The theoretical model developed and demonstrated here can be quite useful for a variety of scientific and applied physics applications, including astrophysics, inertial confinement fusion, and high-energy-density physics where turbulence and mixing have an important role and are challenging to model physically and implement numerically. In the future, additional model validation using simulation and experimental data would be very useful.

Acknowledgments

This work is dedicated to honoring the exemplary scientific career of David L. Youngs. This work was performed under the auspices of the U.S. Department of Energy by Lawrence Livermore National Laboratory under Contract No. DE-AC52-07NA27344.

This document was prepared as an account of work sponsored by an agency of the United States government. Neither the United States government nor Lawrence Livermore National Security, LLC, nor any of their employees makes any warranty, expressed or implied, or assumes any legal liability or responsibility for the accuracy, completeness, or usefulness of any information, apparatus, product, or process disclosed, or represents that its use would not infringe privately owned rights. Reference herein to any specific commercial product, process,

or service by trade name, trademark, manufacturer, or otherwise does not necessarily constitute or imply its endorsement, recommendation, or favoring by the United States government or Lawrence Livermore National Security, LLC. The views and opinions of authors expressed herein do not necessarily state or reflect those of the United States government or Lawrence Livermore National Security, LLC, and shall not be used for advertising or product endorsement purposes.

- [1] Y. Zhou, T. T. Clark, D. S. Clark, S. G. Glendinning, M. A. Skinner, C. M. Huntington, O. A. Hurricane, A. M. Dimits, B. A. Remington, Turbulent mixing and transition criteria of flows induced by hydrodynamic instabilities, *Physics of Plasmas* 26 (2019) 080901–1–080901–68.
- [2] P. C. Duffell, A one-dimensional model for Rayleigh–Taylor instability in supernova remnants, *Astrophysical Journal* 821 (2016) 76–1–76–12.
- [3] L. Welser-Sherrill, J. H. Cooley, D. A. Haynes, D. C. Wilson, M. E. Sherrill, R. C. Mancini, R. Tommasini, Application of fall-line mix models to understand degraded yield, *Physics of Plasmas* 15 (2008) 072702–1–072702–7.
- [4] D. Layzer, On the instability of superposed fluids in a gravitational field, *Astrophysical Journal* 122 (1955) 1–12.
- [5] A. B. Holland-Batt, Two-dimensional motion of particles accelerating in fluids, *Chemical Engineering Research and Design* 50a (1972) 156–167.
- [6] J. Lighthill, *An Informal Introduction to Theoretical Fluid Mechanics*, Oxford University Press, 1988.
- [7] R. Clift, J. R. Grace, M. E. Weber, *Bubbles, Drops, and Particles*, Dover, 2005.
- [8] R. P. Drake, *High-Energy-Density Physics: Fundamentals, Inertial Fusion, and Experimental Astrophysics*, 2nd Edition, Springer, 2018.
- [9] A. Llor, *Statistical Hydrodynamic Models for Developed Mixing Instability Flows*, Springer-Verlag, 2006.
- [10] B. J. Daly, Numerical study of two fluid Rayleigh–Taylor instability, *Physics of Fluids* 10 (1967) 297–307.
- [11] J. Hecht, U. Alon, D. Shvarts, Potential flow models of Rayleigh–Taylor and Richtmyer–Meshkov bubble fronts, *Physics of Fluids* 6 (1994) 4019–4030.
- [12] U. Alon, J. Hecht, D. Ofer, D. Shvarts, Power laws and similarity of Rayleigh–Taylor and Richtmyer–Meshkov mixing fronts at all density ratios, *Physical Review Letters* 74 (1995) 534–537.
- [13] D. L. Youngs, Numerical simulation of mixing by Rayleigh–Taylor and Richtmyer–Meshkov instabilities, *Laser and Particle Beams* 12 (1994) 725–750.
- [14] J. D. Ramshaw, Simple model for linear and nonlinear mixing at unstable fluid interfaces with variable acceleration, *Physical Review E* 58 (1998) 5834–5840.
- [15] G. Dimonte, Spanwise homogeneous buoyancy–drag model for Rayleigh–Taylor mixing and experimental evaluation, *Physics of Plasmas* 7 (2000) 2255–2269.
- [16] G. Dimonte, M. B. Schneider, Density ratio dependence of Rayleigh–Taylor mixing for sustained and impulsive acceleration histories, *Physics of Fluids* 12 (2000) 304–321.
- [17] B. Cheng, J. Glimm, D. H. Sharp, Density dependence of Rayleigh–Taylor and Richtmyer–Meshkov mixing fronts, *Physics Letters A* 268 (2000) 366–374.
- [18] D. Oron, L. Arazi, D. Kartoon, A. Rikanati, U. Alon, D. Shvarts, Dimensionality dependence of the Rayleigh–Taylor and Richtmyer–Meshkov instability late-time scaling laws, *Physics of Plasmas* 8 (2001) 2883–2889.
- [19] L. Arazi, A drag-buoyancy based study of the late-time RT and RM scaling law, Master’s thesis, Tel Aviv University, Tel Aviv, Israel (2001).
- [20] B. Cheng, J. Glimm, D. H. Sharp, Dynamical evolution of Rayleigh–Taylor and Richtmyer–Meshkov mixing fronts, *Physical Review E* 66 (2002) 036312–1–036312–7.
- [21] Y. Srebro, Y. Elbaz, O. Sadot, L. Arazi, D. Shvarts, A general buoyancy–drag model for the evolution of the Rayleigh–Taylor and Richtmyer–Meshkov instabilities, *Laser and Particle Beams* 21 (2003) 347–353.
- [22] B. Cheng, A. J. Scannapieco, Buoyancy–drag mix model obtained by multilayer interpenetration equations, *Physical Review E* 72 (2005) 046310–1–046310–5.
- [23] Y. Cao, W. K. Chow, A theoretical analysis on Rayleigh–Taylor and Richtmyer–Meshkov mixing, *Journal of Physics A* 38 (2005) 6613–6622.
- [24] S. I. Abarzhi, A. Gorobets, K. R. Sreenivasan, Rayleigh–Taylor turbulent mixing of immiscible, miscible and stratified fluids, *Physics of Fluids* 17 (2005) 081705–1–081705–4.
- [25] S. Bouquet, P. Gandeboeuf, P. Pailhoriès, Analytical study of the buoyancy–drag equation, *Mathematical Methods in the Applied Sciences* 30 (2007) 2027–2035.
- [26] K. O. Mikaelian, Nonlinear hydrodynamic interface instabilities driven by time-dependent accelerations, *Physical Review E* 79 (2009) 065303–1–065303–4.
- [27] K. O. Mikaelian, Analytic approach to nonlinear hydrodynamic instabilities driven by time-dependent accelerations, *Physical Review E* 81 (2010) 016325–1–016325–12.
- [28] Y. G. Cao, W. K. Chow, N. K. Fong, Solutions to buoyancy–drag equation for dynamical evolution of Rayleigh–Taylor and Richtmyer–Meshkov mixing zone, *Communications in Theoretical Physics* 56 (2011) 751–755.
- [29] K. O. Mikaelian, Solution to Rayleigh–Taylor instabilities: Bubbles, spikes, and their scalings, *Physical Review E* 89 (2014) 053009–1–053009–7.
- [30] Y. s. Zhang, Z. w. He, F. j. Gao, X. l. Li, B. l. Tian, Evolution of mixing width induced by general Rayleigh–Taylor instability, *Physical Review E* 93 (2016) 063102–1–063102–5.
- [31] P. Ramaprabhu, V. Karkhanis, R. Banerjee, H. Varshochi, M. Khan, A. G. W. Lawrie, Evolution of the single-mode Rayleigh–Taylor instability under the influence of time-dependent accelerations, *Physical Review E* 93 (2016) 013118–1–013118–17.
- [32] S. E. Bouquet, R. Conte, V. Kelsch, F. Louvet, Solutions of the buoyancy–drag equation with a time-dependent acceleration, *Journal of Nonlinear Mathematical Physics* 24 (2017) 3–17.
- [33] J. C. V. Hansom, P. A. Rosen, T. J. Goldsack, K. Oades, P. Fieldhouse, N. W. Cowperthwaite, D. L. Youngs, N. Mawhinney, A. J. Baxter, Radiation driven planar foil instability and mix experiments at the AWE HELEN laser, *Laser and Particle Beams* 8 (1990) 51–71.
- [34] H. Takabe, A. Yamamoto, Reduction of turbulent mixing at the ablation front of fusion targets, *Physical Review A* 44 (1991) 5142–5149.
- [35] T. A. Peyser, P. L. Miller, P. E. Stry, K. S. Budil, E. W. Burke, D. A. Wojtowicz, D. L. Griswold, B. A. Hammel, D. W. Phillion, Measurement of radiation-driven shock-induced mixing from nonlinear initial perturbations, *Physical Review Letters* 75 (1995) 2332–2335.
- [36] G. Dimonte, M. Schneider, Turbulent Richtmyer–Meshkov instability experiments with strong radiatively driven shocks, *Physics of Plasmas* 4 (1997) 4347–4357.
- [37] P. A. Amendt, J. D. Colvin, R. E. Tipton, D. E. Hinkel, M. J. Edwards, O. L. Landen, J. D. Ramshaw, L. J. Suter, W. S. Varnum, R. G. Watt, Indirect-drive noncryogenic double-shell ignition targets for the National Ignition Facility: Design and analysis, *Physics of Plasmas* 9 (2002) 2221–2233.
- [38] K. Rifai, F. Vidal, T. W. Johnston, Theoretical investigation of the Rayleigh–Taylor instability in laser-produced plasmas driving into background gases, *Physics of Plasmas* 14 (2007) 082311–1–082311–10.
- [39] A. R. Miles, Nonlinear Rayleigh–Taylor instabilities in fast Z pinches, *Physics of Plasmas* 16 (2009) 032702–1–032702–11.
- [40] V. Rana, H. Lim, J. Melvin, J. Glimm, B. Cheng, D. H. Sharp, Mixing with applications to inertial-confinement-fusion implosions, *Physical Review E* 95 (2017) 013203–1–013203–13.
- [41] C. M. Huntington, A. Shimony, M. Trantham, C. C. Kuranz, D. Shvarts, C. A. D. Stefano, F. W. Doss, R. P. Drake, K. A. Flippo, D. H. Kalantar, S. R. Klein, J. L. Kline, S. A. MacLaren, G. Malamud, A. R. Miles, S. T. Prisbrey, K. S. Raman, B. A. Remington, H. F. Robey, W. C. Wan, H.-S. Park, Ablative stabilization of Rayleigh–Taylor instabilities resulting from a laser-driven radiative shock, *Physics of Plasmas* 25 (2018) 052118–1–052118–9.
- [42] A. R. Miles, The effect of initial conditions on the nonlinear evolution of perturbed interfaces driven by strong blast waves, Ph.D. thesis, University of Maryland, College Park, MD (2004).
- [43] A. R. Miles, Bubble merger model for the nonlinear Rayleigh–Taylor instability driven by a strong blast wave, *Physics of Plasmas* 11 (2004) 5140–5155.
- [44] A. R. Miles, The blast-wave-driven instability as a vehicle for understanding supernova explosion structure, *Astrophysical Journal* 696 (2009) 498–514.
- [45] M. T. H. de Frahan, Numerical simulations of shock and rarefaction waves

interacting with interfaces in compressible multiphase flows, Ph.D. thesis, University of Michigan, Ann Arbor, MI (2016).

- [46] K. Balakrishnan, S. Menon, A multiphase buoyancy-drag model for the study of Rayleigh-Taylor and Richtmyer-Meshkov instabilities in dusty gases, *Laser and Particle Beams* 29 (2011) 201–217.
- [47] K. Balakrishnan, On bubble and spike oscillations in a dusty gas Rayleigh-Taylor instability, *Laser and Particle Beams* 30 (2012) 633–638.
- [48] K. Balakrishnan, Explosion-driven Rayleigh-Taylor instability in gas-particle mixtures, *Physics of Fluids* 26 (2014) 043303–1–043303–15.
- [49] D. Shvarts, O. Sadot, D. Oron, A. Rikanati, U. Alon, *Handbook of Shock Waves*, Vol. 2, Academic Press, 2001, Ch. 14, pp. 489–543.
- [50] B. Cheng, Review of turbulent mixing models, *Acta Mathematica Scientia* 29 (2009) 1703–1720.
- [51] Y. Zhou, G. B. Zimmerman, E. W. Burke, Formulation of a two-scale transport scheme for the turbulent mix induced by Rayleigh-Taylor and Richtmyer-Meshkov instabilities, *Physical Review E* 65 (2002) 056303–1–056303–6.
- [52] G. Dimonte, R. Tipton, *K-L* turbulence model for the self-similar growth of the Rayleigh-Taylor and Richtmyer-Meshkov instabilities, *Physics of Fluids* 18 (2006) 085101–1–085101–22.
- [53] R. M. Davies, G. I. Taylor, The mechanics of large bubbles rising through extended liquids and through liquids in tubes, *Proceedings of the Royal Society of London A* 200 (1950) 375–390.
- [54] B. E. Morgan, M. E. Wickett, Three-equation model for the self-similar growth of Rayleigh-Taylor and Richtmyer-Meshkov [sic] instabilities, *Physical Review E* 91 (2015) 043002–1–043002–9.
- [55] O. Schilling, Reynolds-averaged Navier-Stokes modeling of turbulent Rayleigh-Taylor, Richtmyer-Meshkov, and Kelvin-Helmholtz mixing using a higher-order shock-capturing method, in: *Proceedings of the ASME - JSME - KSME Joint Fluids Engineering Conference 2019*, American Society of Mechanical Engineers, 2019, pp. AJKFLUIDS2019–5235.
- [56] J. T. Mórán-López, O. Schilling, Multicomponent Reynolds-averaged Navier-Stokes simulations of reshocked Richtmyer-Meshkov instability-induced mixing, *High Energy Density Physics* 9 (2013) 112–121.
- [57] J. T. Mórán-López, O. Schilling, Multi-component Reynolds-averaged Navier-Stokes simulations of Richtmyer-Meshkov instability and mixing induced by reshock at different times, *Shock Waves* 24 (2014) 325–343.
- [58] M. M. Rogers, R. D. Moser, Direct simulation of a self-similar turbulent mixing layer, *Physics of Fluids* 6 (2018) 903–923.
- [59] S. B. Pope, *Turbulent Flows*, Cambridge University Press, 2000.
- [60] D. M. Snider, M. J. Andrews, The simulation of mixing layers driven by compound buoyancy and shear, *ASME Journal of Fluids Engineering* 118 (1996) 370–376.
- [61] B. E. Morgan, O. Schilling, T. A. Hartland, Two-length-scale turbulence model for self-similar buoyancy-, shock-, and shear-driven mixing, *Physical Review E* 97 (2018) 013104–1–013104–18.
- [62] J. Crank, *The Mathematics of Diffusion*, 2nd Edition, Oxford University Press, 1975.
- [63] K. O. Mikaelian, Testing an analytic model for Richtmyer-Meshkov turbulent mixing widths, *Shock Waves* 25 (2015) 35–45.
- [64] G. L. Brown, A. Roshko, On density effects and large structure in turbulent mixing layers, *Journal of Fluid Mechanics* 64 (1974) 775–816.